

Optical Engineering

OpticalEngineering.SPIEDigitalLibrary.org

Influence of beam shape on piston and tilt error in coherent combined laser array

Przemyslaw Gontar
Jan K. Jabczynski

Influence of beam shape on piston and tilt error in coherent combined laser array

Przemyslaw Gontar* and Jan K. Jabczynski

Military University of Technology, Institute of Optoelectronics, Warsaw, Poland

Abstract. An analysis of beam combining quality and the influence of beam profile on tilt and piston error tolerances is presented. We define beam combining performance metrics in terms of powers contained within a specific radius. It is shown that the selection of this radius has a significant effect on the obtained tolerance values. We have taken the tolerance limit as a decrease in intensity of 20%, for piston and tilt error. In addition, for the tilt error, as tolerance limit, we have taken a pointing error equal to the diffraction limit. Our analysis demonstrates that the beam combining performance metric based on the diffraction-limited radius functions best for describing the impact of aberrations on the coherent combined laser array optical system. Our results lead to two important conclusions. First, the tilt error has a greater impact on the degradation of beam quality. Second, a Gaussian beam has greater tolerance for both errors than a top-hat beam. © The Authors. Published by SPIE under a Creative Commons Attribution 4.0 Unported License. Distribution or reproduction of this work in whole or in part requires full attribution of the original publication, including its DOI. [DOI: [10.1117/1.OE.58.6.066103](https://doi.org/10.1117/1.OE.58.6.066103)]

Keywords: lasers; beam combining; tilt error; piston error; simulation.

Paper 190318 received Mar. 7, 2019; accepted for publication May 16, 2019; published online Jun. 6, 2019.

1 Introduction

High average power lasers have found their application in materials processing,¹ defense systems,^{2,3} and fundamental research.⁴ The challenge is not only to obtain multi-kilowatt output power but also to maintain near diffraction-limited beam quality. Solid-state lasers deserve special attention due to their compactness, performance, and reliability.⁵ However, the development of the power scaling of such lasers has thus far been hampered by beam-quality degradation due to thermo-optical phenomena.^{6–8} To date, several-kilowatt average powers from single-aperture solid-state lasers have been demonstrated.^{9–11}

Another approach for power scaling is to use multiple lasers with relatively small output powers and combine them to obtain a single-aperture laser propagation characteristic. This class of techniques is called laser beam combining, and it can be divided into two general groups: coherent beam combining (CBC) and wavelength beam combining (WBC).¹² In CBC, all the individual beams must be mutually coherent, and this type of beam combining technique can be subdivided into two classes depending on the configuration used: side-by-side (tiled aperture), for which the divergence angle is reduced but the beam size is increased with respect to each individual beam, or filled-aperture, in which a beam combining element is used to obtain a single beam of the same beam size and divergence as the individual beams from which it is constructed. A special case of beam combining is when the phase of the array of beams is not controlled, which leads to incoherent beam combining (IBC). In WBC, mutual coherence is not required, and the emitters have nonoverlapping optical spectra and are combined at wavelength-sensitive beam combiner. Unlike CBC, the output beam is not monochromatic, which renders the technique inappropriate for some applications. Increasing power

density while maintaining beam quality can be achieved only via CBC or WBC, where upon increasing the number of emitters in the array, the beam divergence angle remains unchanged. The reverse situation occurs in IBC; beam divergence increases with the number of beams in the array and beam

quality decreases. Many successful CBC^{13–15} and WBC^{16–18} implementations have already been reported in the literature.

An advantage of WBC is that it does not require mutual coherence, which makes it easier to reach stable operation. The utilization of a beam combiner element results in additional dissipative losses. This limitation disappears in the case of CBC in a tiled-aperture configuration. However, side-by-side beam arrays require the control of a larger number of parameters, which can easily result in beam-quality degradation.¹⁹ The errors associated with this degradation can be divided into two groups: geometric, related to array architecture, and nongeometric, related to the quality of the coherent combining system. The most important representatives of the latter group are phase mismatch (piston error) and tilt errors. These low-order aberrations cause energy spreading into the side lobes and distortion of the main lobe in far-field irradiance patterns. To achieve effective beam combining, piston and tilt errors must be controlled with high accuracy, to a fraction of a wavelength.

2 Model

2.1 Coherent Beam Arrays in the Far Field

The amplitude of an array composed of N laser subapertures in the near field is defined as follows:

$$A_{nf,N}(x_{nf}, y_{nf}) = \sum_{m=1}^N A_{nf,m}(x_{nf} - \alpha_m, y_{nf} - \beta_m), \quad (1)$$

where (α_m, β_m) and $A_{nf,m}(x_{nf}, y_{nf})$ are subaperture center coordinates and the amplitude function of m -th subaperture,

*Address all correspondence to Przemyslaw Gontar, E-mail: przemyslaw.gontar@wat.edu.pl

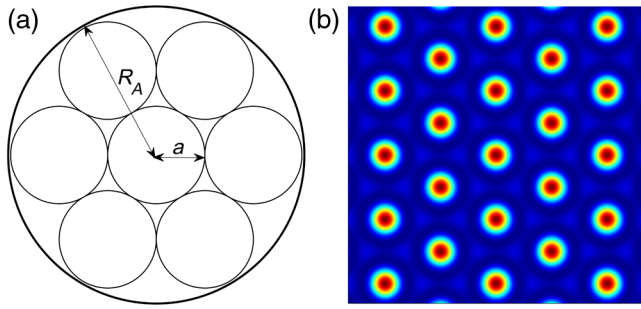


Fig. 1 (a) Hexagonal array with seven beamlets and (b) corresponding far-field summation pattern.

respectively. Assuming the paraxial approximation and identical subapertures, the diffraction pattern is described as a Fourier transform of the individual subaperture function multiplied by an array in the same configuration as the point source pattern.²⁰ In this case, the intensity in the far field at the focal point f is expressed as

$$I_{ff,N}(x_{ff}, y_{ff}) = |A_{ff}(x_{ff}, y_{ff})|^2 \cdot \left| \sum_{m=1}^N \sum_{n=1}^N \mu_{mn} \cdot \exp \left\{ \frac{ik}{f} [x_{ff}(\alpha_m - \alpha_n) + y_{ff}(\beta_m - \beta_n)] \right\} \right|, \quad (2)$$

where $A_{ff}(x_{ff}, y_{ff})$ is the Fourier transform of the individual subaperture function, $k = 2\pi/\lambda$ is the wavenumber, λ is the wavelength, and a is the subaperture radius; $\mu_{m,n}$ is the degree of coherence between the m -th and n -th beams, which takes the values $\mu = 1$ for full coherence, $0 < \mu < 1$ for partial coherence, and $\mu_{m,n} = \delta_{m,n}$ (the Kronecker delta) for incoherence. To simulate the physical problem, we used spatial coordinates proportional to λ/R_A , where R_A is the array aperture radius. Considering Eq. (2), it is apparent that the form of the summation part depends on the centers of the apertures, and the resulting intensity will take a different form for each array symmetry. The pattern of the

summation for hexagonal symmetry [Fig. 1(a)] is shown in Fig. 1(b).

2.2 Beam Profile

The amplitude in near field within each subaperture is described by a super-Gaussian (SG) function as follows:²¹

$$A_{nf}(r_{nf}) = c_{\text{norm}} \cdot \exp \left[- \left(\frac{r_{nf}}{w_0} \right)^{2p} \right], \quad (3)$$

where w_0 is the beam radius, p is the order of the SG, $r_{nf}^2 = x_{nf}^2 + y_{nf}^2$ defines the radial coordinate, and c_{norm} is a normalization factor; the latter takes the form

$$c_{\text{norm}} = 1 / \int_0^{1.5a} |A_{nf}(r_{nf})|^2 r_{nf} dr_{nf}. \quad (4)$$

In the case of radial symmetry, to calculate the amplitude in the far field, a Hankel transform may be used as follows:

$$A_{ff}(r_{ff}) = \int_0^a J_0 \left(\frac{kr_{ff}r_{nf}}{f} \right) \cdot A_{nf} \cdot r_{nf} dr_{nf}. \quad (5)$$

In our analysis, we considered three cases of input amplitude, $p = \{1, 3, 32\}$, which correspond to Gaussian, super-Gaussian, and approximate top-hat distributions, respectively. To get the best subaperture filling factor, beam radii were selected so that the power inside the aperture, which was normalized to unity, corresponded to the maximum possible w_0 with an accuracy of 0.005. The determined beam radii are $w_0 = \{0.513a, 0.847a, 0.994a\}$. Intensity cross sections are presented for the near and far fields in Figs. 2(a) and 2(b), respectively. Figure 3 shows the influence of beam shape on a far-field CBC intensity pattern, using normal and logarithmic scales, for a hexagonal array [Fig. 1(a)].

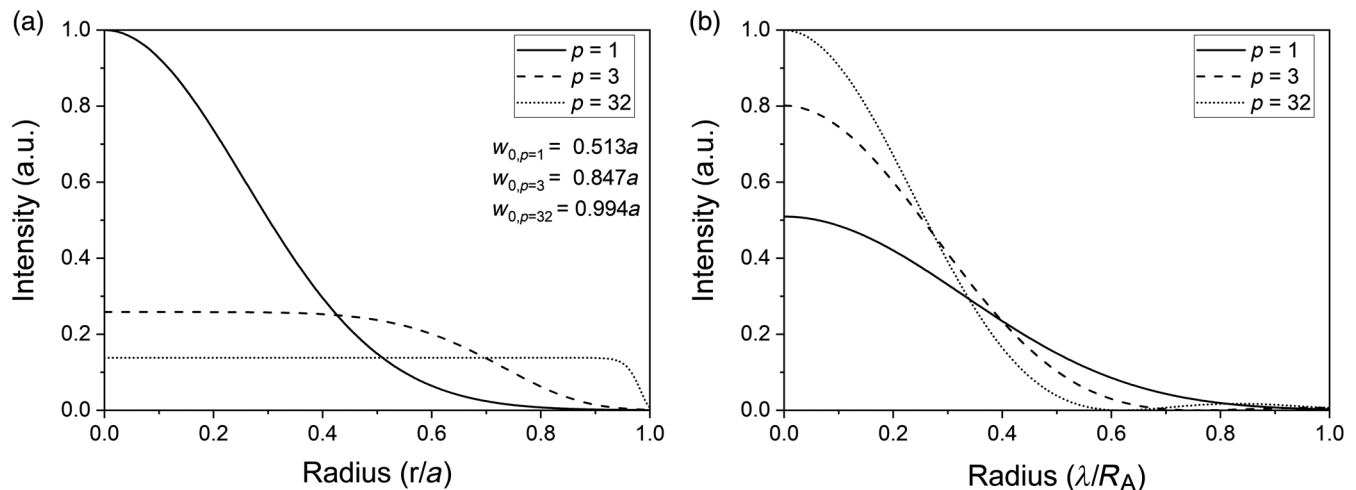


Fig. 2 Normalized intensity cross sections for $p = \{1, 3, 32\}$ in (a) the near field and (b) the far field.

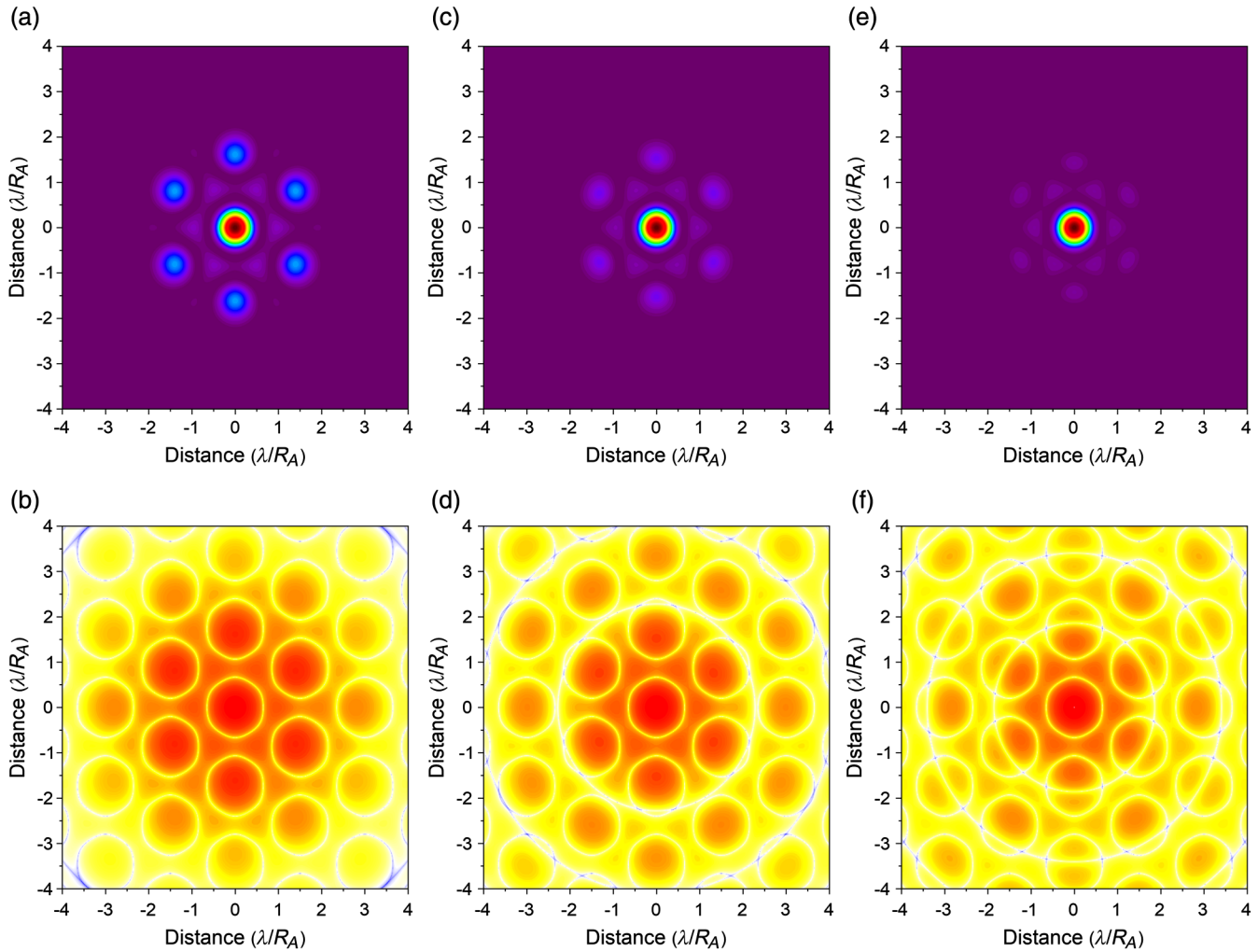


Fig. 3 Far-field intensity pattern in linear (top) and logarithmic (bottom) intensity color scales for a hexagonal array of seven Gaussian-type beamlets with (a, b) $p = 1$ – Gaussian, (c, d) $p = 3$ – super-Gaussian, and (e, f) $p = 32$ – approximate top-hat distribution.

2.3 Beam Combining Performance

The intensity distribution in the far field for CBC always has side lobes due to the incomplete filling of the exit aperture. The use of classical parameters to describe the beam, such as the beam quality parameter M^2 and Strehl ratio SR,²² have been unsuccessful due to their failure to use all of the information contained in beam profile in the far field. M^2 increases with number of emitters in the laser array and does not include the side lobes. SR, on the other hand, contains information about the on-axis peak intensity, not the energy encircling the peak in the main lobe.²³ To account for all factors, we use a power in the bucket (PIB) distribution, defined as²²

$$PIB(r_b) = \frac{\int_0^{r_b} \int_0^{2\pi} I_{ff} \cdot r_b dr_b d\varphi}{\int_0^\infty \int_0^{2\pi} I_{ff} \cdot r_b dr_b d\varphi}. \quad (6)$$

In previous work,²⁴ we showed that metrics based on the horizontal PIB (HPIB) or vertical PIB (VPIB) were not able to describe CBC performance well. Because factors describing quality based on the PIB distribution were not well established, we proposed three metrics defined as follows:

$$I_{86.5\%} = \frac{P_{86.5\%}}{R_{86.5\%}^2}, \quad (7)$$

which is the ratio of 86.5% of the total power ($P_{86.5\%} = 0.865$) within the corresponding radius $R_{86.5\%}$ and that radius

$$I_{0mode} = \frac{P_{0mode}}{R_{0mode}^2}, \quad (8)$$

the ratio of the power inside the main lobe P_{0mode} ; within the corresponding radius R_{0mode} and that radius, which is defined as the first inflection point of the PIB curve; and

$$I_{dl} = \frac{P_{dl}}{R_{dl}^2}, \quad (9)$$

the ratio of the power P_{dl} inside the circle with radius R_{dl} and that radius, which corresponds to the diffraction limit $0.75\lambda/R_A$ for which the PIB $\approx 86.5\%$ for the “top hat” amplitude function in the near field.

PIB curves (for the intensity patterns shown in Fig. 3) with marked bucket radii are given in Fig. 4. The values

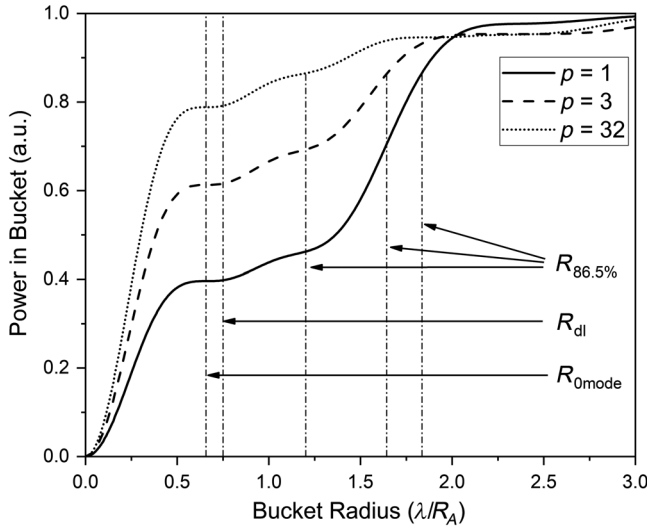


Fig. 4 PIB distribution for the three cases of beam shape shown in Fig. 3, $p = 1$ (solid line), $p = 3$ (dashed line), and $p = 32$ (dotted line); the bucket radii for all three proposed metrics are indicated by vertical lines.

Table 1 Parameter values for each of the three metrics for the PIB curves shown in Fig. 4.

	$p = 1$	$p = 3$	$p = 32$
$R_{86.5\%}$	1.836	1.643	1.202
$P_{86.5\%}$	0.865	0.865	0.865
$I_{86.5\%}$	0.257	0.320	0.598
R_{0mode}	0.657	0.657	0.657
P_{0mode}	0.396	0.613	0.788
I_{0mode}	0.917	1.419	1.825
R_{dl}	0.750	0.750	0.750
P_{dl}	0.398	0.616	0.791
I_{dl}	0.708	1.095	1.406

determined for the three metrics are summarized in Table 1, and they demonstrate that the quality of the beam combining is better for beam shapes similar to the top-hat shape.

3 Impact of Piston Error

Piston error, otherwise known as phase error, is the difference in the optical path of each element of the laser array and is equivalent to the delays between the subapertures of the wavefront.^{25,26} A visualization of this effect is shown in Fig. 5. Piston error results from the fact that the use of phase locking for each channel does not allow cancellation of the relative phase between the elements of the laser array. This error also includes the effects of the



Fig. 5 Three-dimensional (3-D) visualization of piston error for a hexagonal beam array.

mechanical accuracy of optomechanical elements, thermal factors, and the experimental environment.¹⁹

Considering the piston error, the intensity in the far field takes the form

$$I_{ff,N}(x_{ff}, y_{ff}) = |A_{ff}(x_{ff}, y_{ff})|^2 \cdot \left| \sum_{m=1}^N \sum_{n=1}^N \mu_{mn} \cdot \exp\left\{ \frac{ik}{f} [x_{ff}(\alpha_m - \alpha_n) + y_{ff}(\beta_m - \beta_n)] \right\} \cdot \exp(i\Delta\varphi_{m,n}) \right|, \quad (10)$$

where $\Delta\varphi_{m,n} = |\varphi_m - \varphi_n|$ is the phase difference between the m 'th and n 'th beamlets. By analyzing Eq. (10), we can conclude that the phase mismatch results in distortions and shifts of cosine minima and maxima. Consequently, energy can be dissipated within a limited area defined by the beam shape function $|A_{ff}(x_{ff}, y_{ff})|^2$.

Our simulations were performed for three cases of beam shape, for $p = \{1, 3, 32\}$ with corresponding $w_0 = \{0.513a, 0.847a, 0.994a\}$. Piston error c was drawn from a uniform distribution in the range $(-c, c)$, where $c \in (0, 3\lambda/5)$. For each c , 500 attempts were made, and the intensity profiles were averaged.

The three metrics we defined, $I_{86.5\%}$, I_{0mod} , and I_{dl} as well as SR for comparison, each normalized to unity, are shown in Fig. 6 as functions of the rms phase mismatch $\Delta\varphi_{RMS}$. According to the Maréchal criterion, the tolerance of the wavefront aberration error in a diffraction-limited optical system occurs for SR above 80%.²⁷ We have extended this assumption to the metrics we propose. Consequently, as an acceptable error for the optical system, we consider one for which the power contained in a given radius does not fall below 80%. The values we determined for the permissible $\Delta\varphi_{RMS}$ of the limiting case are presented in Table 2. Figure 6(a) shows that the $I_{86.5\%}$ parameter cannot be used to determine beam combining performance due to the lack of correlation between curves depending on the parameter p . I_{0mod} and I_{dl} , on the other hand, show correlations with the p

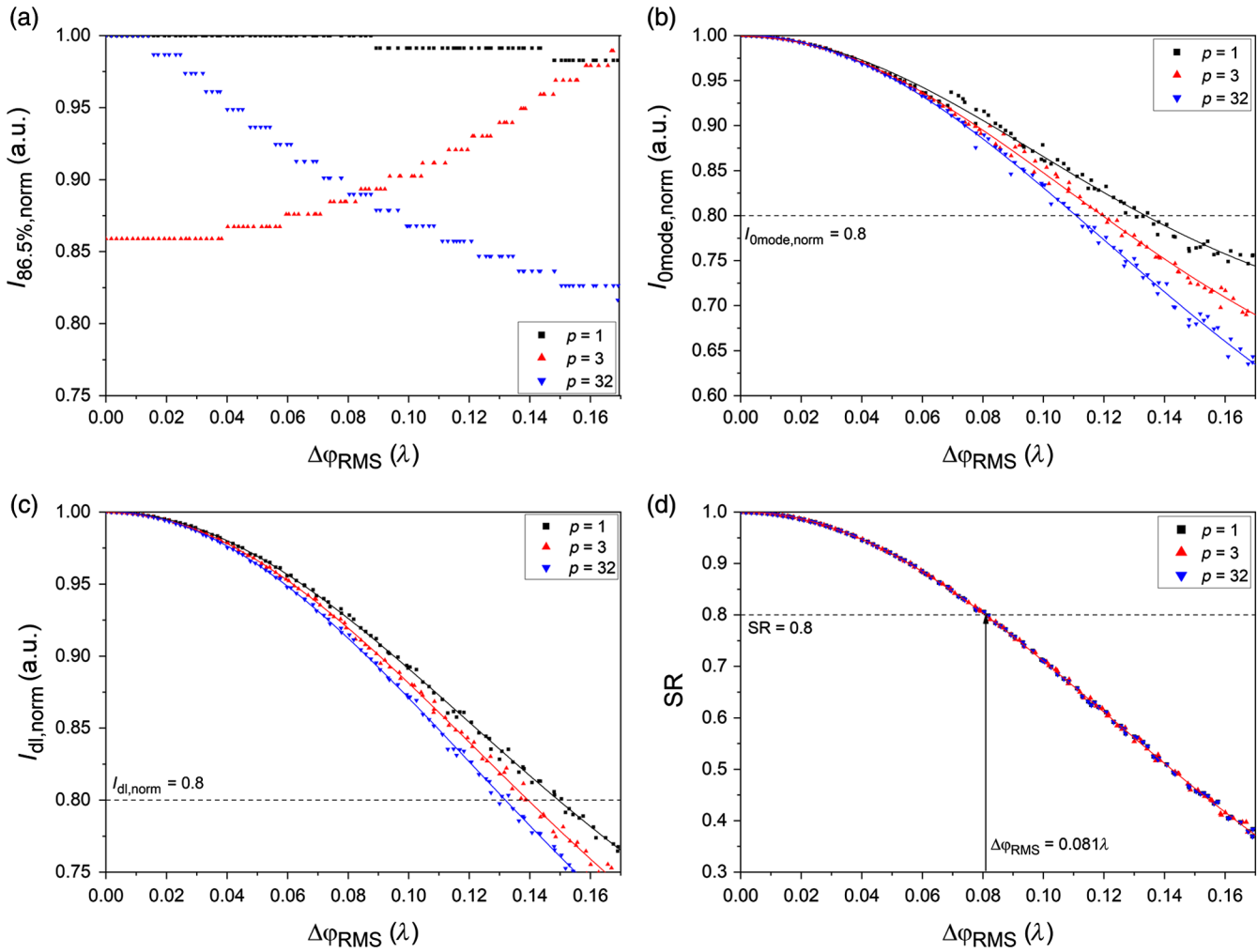


Fig. 6 (a) $I_{86.5\%}$, (b) I_{0mode} , (c) I_{dl} , and (d) SR as functions of rms piston error for $p = 1$ (black squares), $p = 3$ (red triangles), and $p = 32$ (blue triangles).

Table 2 Determined values of admissible rms piston error for SR, I_{0mode} , and I_{dl} for which the power limited in a given radius does not fall below 80%, for three cases of the parameter p .

	$\Delta\varphi_{RMS,SR}$	$\Delta\varphi_{RMS,0mode}$	$\Delta\varphi_{RMS,dl}$
$p = 1$	0.081	0.134	0.149
$p = 3$	0.081	0.119	0.139
$p = 32$	0.081	0.111	0.133

parameter and can be approximated by the curve $y = a \cdot \exp[b \cdot (x)^2] + c$, which is similar to the one describing SR. Both for I_{0mode} and I_{dl} , the piston error tolerance is higher in the case of a value of smaller p . This may be because for the smaller p , less energy is contained within the main diffraction lobe, which translates into a lower susceptibility to changes in the cosine function amplitude in the summation in Eq. (10) because of the piston error. Figure 6(d) shows that the shape of the laser beam does not affect the SR parameter, which disqualifies it as a potential metric for beam combining performance.

Different PIB curves for various rms piston errors are presented in Fig. 7. These plots show that as the error increases, the curves begin to resemble those resulting of the amplitude function. In addition, the energy of the side lobes increases at the cost of the main lobe from which it is dissipated.

Intensity profiles for rms piston error corresponding $I_{dl} = 0.8$ for $p = \{1, 3, 32\}$ are presented in Fig. 8 in normal linear (top) and logarithmic (bottom) intensity color scales.

4 Impact of Tilt Error

Tilt errors result from the accuracy of optomechanical components, and they cause errors in the relative far-field beam pointing of the elements.²⁸ To achieve effective beam combining, this error must be controlled at the level of a fraction of the wavelength. Tilt can be visualized as a tilt of the wavefront in the near field, as illustrated schematically in Fig. 9.

In Fourier space, the tilt of the wavefront by an angle θ is equivalent to shifting the image from the center by $f \tan \theta$. The amplitude coming from the m 'th beamlet of the aperture therefore takes the form

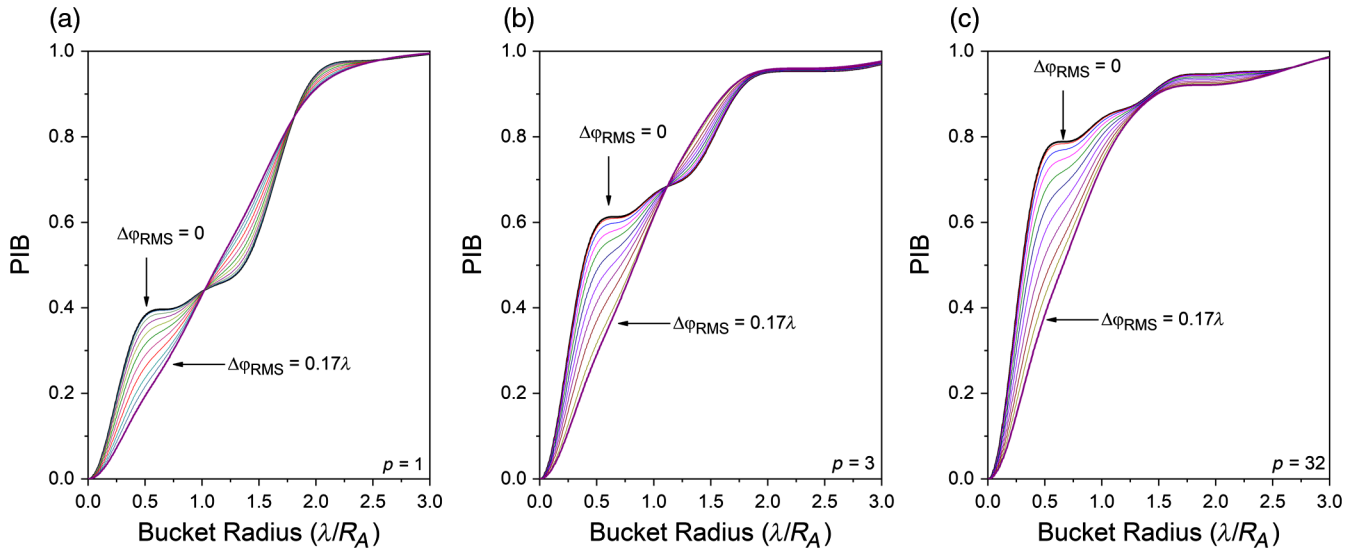


Fig. 7 PIB distribution for selected rms piston error as a function of dimensionless bucket radius for (a) $p = 1$, (b) $p = 3$, and (c) $p = 32$.

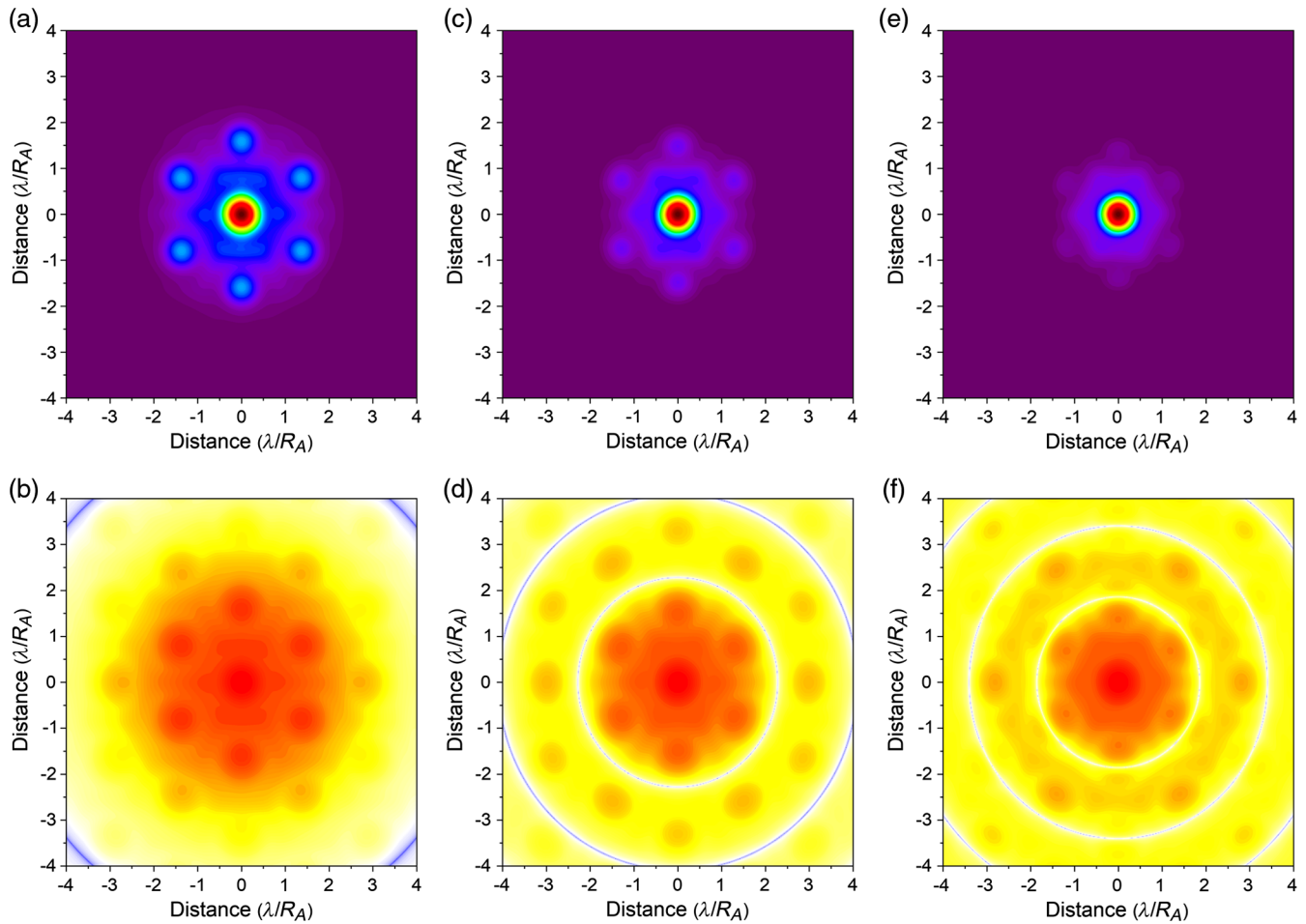


Fig. 8 Far-field intensity pattern with rms piston error corresponding to $I_{d1} = 0.8$ in linear (top) and logarithmic (bottom) intensity color scales for a hexagonal array of seven Gaussian-type beamlets with (a, b) $p = 1$ - Gaussian, (c, d) $p = 3$ - super-Gaussian, and (e, f) $p = 32$ - approximate top-hat distribution.



Fig. 9 3-D visualization of tilt error for a hexagonal beam array.

$$A_{ff,m,\text{tilt}}(x_{ff}, y_{ff}) = A_{ff}(x_{ff}, y_{ff}) * \delta[x_{ff} - f \tan(\theta_{x,m}), y_{ff} - f \tan(\theta_{y,m})], \quad (11)$$

where $*$ is the convolution operator and δ is the Dirac delta function. From Eq. (11), it follows that each subaperture of

the laser array has a different amplitude function, therefore, it cannot be separated before the summation factor in Eq. (2). In this case, the intensity at the focal point takes the form

$$I_{ff,N}(x_{ff}, y_{ff}) = \left| \sum_{m=1}^N \sum_{n=1}^N \mu_{mn} \cdot A_{ff,m,\text{tilt}}(x_{ff}, y_{ff}) \cdot A_{ff,n,\text{tilt}}(x_{ff}, y_{ff}) \cdot \exp\left\{\frac{ik}{f}[x_{ff}(\alpha_m - \alpha_n) + y_{ff}(\beta_m - \beta_n)]\right\} \right|. \quad (12)$$

Analysis of Eq. (12) leads us to the conclusion that tilt error causes an overlapping of the amplitude function, which in turn leads to a spreading of the beam profile intensity in the far field.

Simulations were carried out for the same p and w_0 parameters as in the case of piston error. Shifts in the x and y directions, Δx and Δy , respectively, have been drawn from a uniform random distribution so that $\Delta x, \Delta y \in (-d, d)$ where $d \in (0, R_{86.5\%})$ and $\Delta s = \sqrt{(\Delta x)^2 + (\Delta y)^2}$. For each d , 500 attempts were made, and intensity profiles were averaged. Because Δs depends on λ , f , and R_A , instead of the angle, we used a shift distance in dimensionless units.

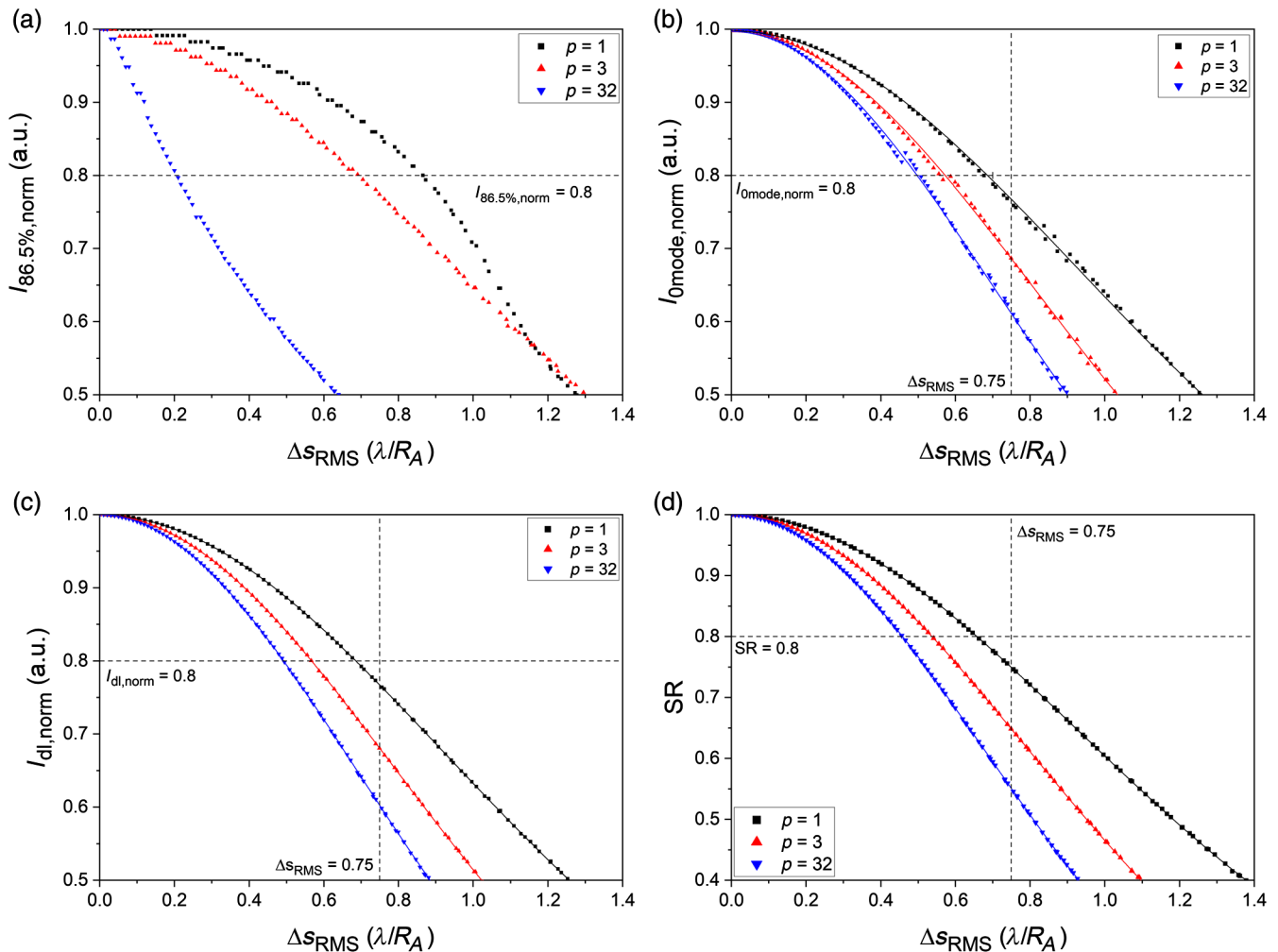


Fig. 10 (a) $I_{86.5\%}$, (b) $I_{0\text{mode}}$, (c) I_{dl} , and (d) SR as functions of rms tilt error for $p = 1$ (black squares), $p = 3$ (red triangles), and $p = 32$ (blue triangles).

Table 3 Determined values of admissible rms pointing errors for SR, $I_{86.5\%}$, $I_{0\text{mode}}$, and I_{dl} for three cases of the parameter p for which the power limited in a given radius does not fall below 80% and intensity values for the diffraction-limited shift $\Delta s_{\text{RMS}} = 0.75$.

Δs_{RMS} for $I = 0.8$				
	$\Delta s_{\text{RMS},86.5\%}$	$\Delta s_{\text{RMS},0\text{mode}}$	$\Delta s_{\text{RMS},\text{dl}}$	$\Delta s_{\text{RMS},\text{SR}}$
$p = 1$	0.865	0.685	0.685	0.658
$p = 3$	0.691	0.571	0.568	0.537
$p = 32$	0.209	0.497	0.492	0.448
I for $\Delta s_{\text{RMS}} = 0.75$				
	$I_{86.5\%}$	$I_{0\text{mode}}$	I_{dl}	SR
$p = 1$	—	0.767	0.767	0.749
$p = 3$	—	0.686	0.681	0.648
$p = 32$	—	0.611	0.602	0.542

The angle of rms tilt error can then be calculated using the expression $\theta = \arctan(\Delta s \lambda / R_A)$.

Figure 10 shows the dependence of the parameters $I_{86.5\%}$, $I_{0\text{mode}}$, I_{dl} , and SR on rms pointing error Δs_{RMS} . We have, in addition, determined the intensity value for which Δs_{RMS} is within the range of the diffraction limit $0.75\lambda/R_A$. Similar to the case of piston error, the dependence of $I_{86.5\%}$ on Δs_{RMS} [Fig. 10(a)] does not take the same function for the three different p . However, for the parameters $I_{0\text{mode}}$, I_{dl} , and SR, in each case of p , a curve of the type $y = a \cdot \exp[b \cdot (x)^2] + c$, may be fitted to the plot; this situation is identical to that of the piston error analysis. In addition, the Gaussian beam ($p = 1$) seems to have a greater tolerance to the tilt error. This may be because a larger surface area is occupied by this beam than that of the $p = 32$ beam (top-hat) beam, as given by its Fourier transform, and thus the overlapping

amplitudes are much smaller for $p = 1$. The values of Δs_{RMS} determined for $I_{86.5\%}$, $I_{0\text{mode}}$, and I_{dl} when SR = 0.8, and of $I_{0\text{mode}}$, I_{dl} , and SR when $\Delta s_{\text{RMS}} = 0.75$ are listed in Table 3.

PIB curves for each p are presented in Fig. 11. In comparison to the piston error, as the pointing error increases, the PIB curve is shifted, and there is some degradation.

Intensity profiles for rms tilt error corresponding $I_{\text{dl}} = 0.8$ for $p = \{1, 3, 32\}$ are presented in Fig. 12 in normal linear (top) and logarithmic (bottom) intensity color scales.

5 Conclusion

An analysis of beam combining performance and the influence of beam profile on tilt and piston error tolerances have been presented. As a result, the metrics $I_{0\text{mode}}$ and I_{dl} were observed to effectively describe CBC performance. However, while in the case of tilt error, these two functions are well defined, in the case of piston error $I_{0\text{mode}}$ is not well determined. This is because $R_{0\text{mode}}$ is determined numerically and a for large rms piston error, the main lobe is barely discernable and the calculated value of $I_{0\text{mode}}$ is subject to a large error.

For best CBC performance without the presence of errors, the top-hat beam is better than Gaussian beam, because more energy is contained in main lobe. On the other hand, our analysis of piston and tilt errors shows that the Gaussian beam has a higher tolerance for piston and tilt errors than those similar with profiles similar to a top-hat. For the piston error, acceptable errors for $I_{\text{dl}} = 0.8$ are $\Delta \varphi_{\text{RMS},p=1} = 0.149\lambda$, $\Delta \varphi_{\text{RMS},p=3} = 0.139\lambda$, and $\Delta \varphi_{\text{RMS},p=32} = 0.133\lambda$. For the tilt error, rms pointing errors are $\Delta s_{\text{RMS},p=1} = 0.685\lambda/R_A$, $\Delta s_{\text{RMS},p=3} = 0.568\lambda/R_A$, and $\Delta s_{\text{RMS},p=32} = 0.492\lambda/R_A$. The intensity for the diffraction-limited rms pointing error, $\Delta s_{\text{RMS}} = 0.75\lambda/R_A$, drops as p increases from $I_{\text{dl},p=1} = 0.767$, to $I_{\text{dl},p=3} = 0.681$, and $I_{\text{dl},p=32} = 0.602$. For the piston error, this may be due to a lower power content in main lobe, which is less susceptible to changes in the difference between the maximum and the minimum of the cosine function. However, in the case of tilt error, the greater tolerance may result from the Gaussian function than the

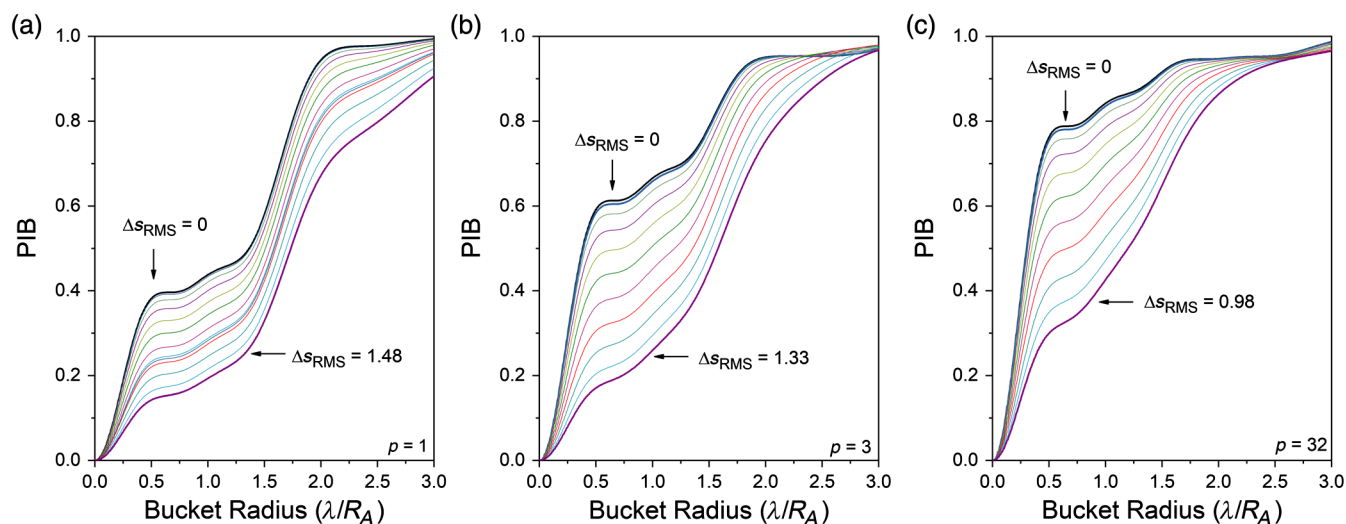


Fig. 11 PIB distribution for selected rms tilt errors as a function of dimensionless bucket radius for (a) $p = 1$, (b) $p = 3$, and (c) $p = 32$.

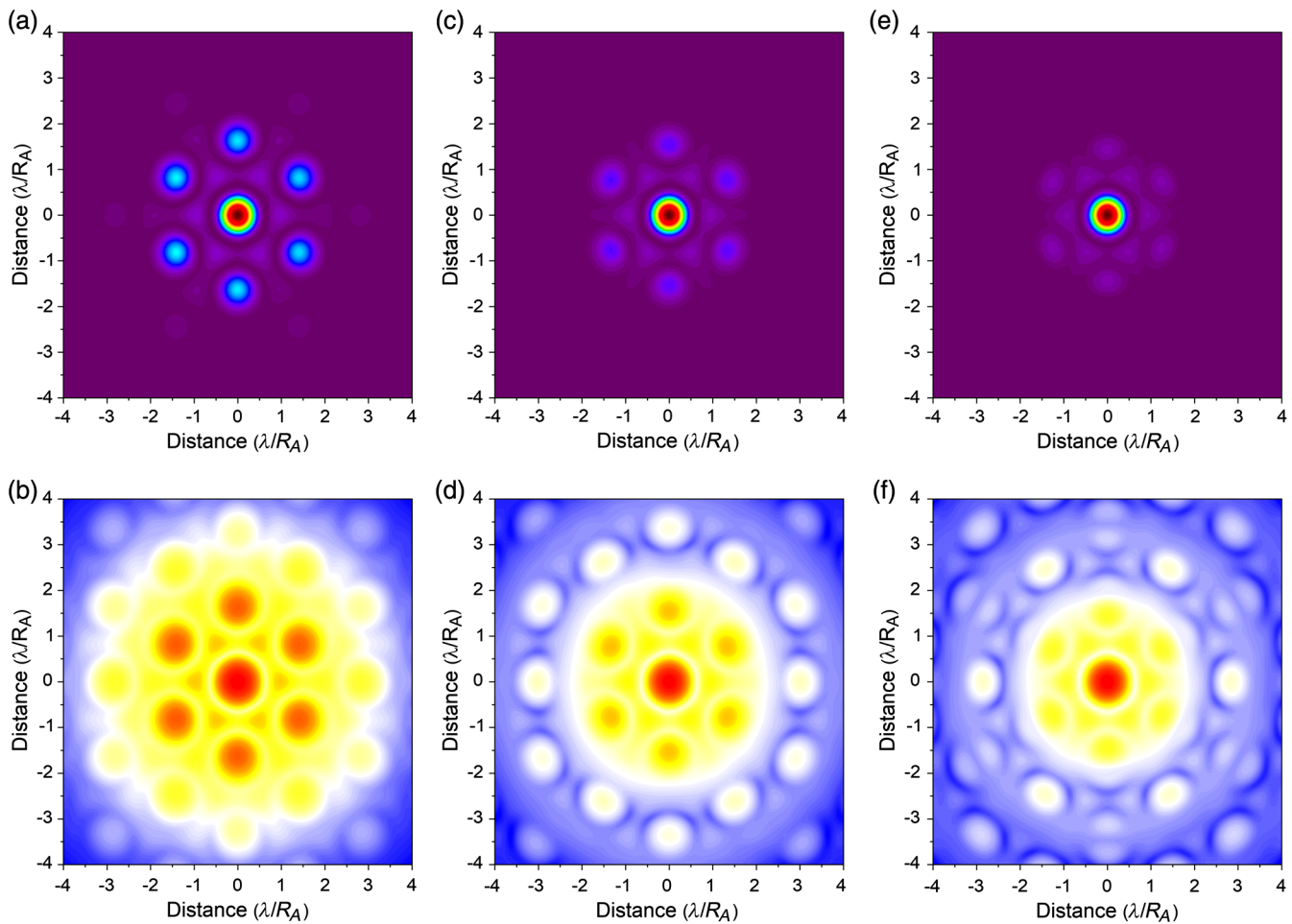


Fig. 12 Far-field intensity pattern with rms tilt error corresponding to $I_{dl} = 0.8$ in linear (top) and logarithmic (bottom) intensity color scales for a hexagonal array of seven Gaussian-type beamlets with (a, b) $p = 1$ – Gaussian, (c, d) $p = 3$ – super-Gaussian, and (e, f) $p = 32$ – approximate top-hat distribution.

(sombbrero) $2J_1(x)/x$ function, which results in the overlap of amplitudes being smaller.

Acknowledgments

The work was financed by the National Centre for Research and Development of Poland in the framework of strategic program DOB-1-6/1/PS/2014.

References

1. J. F. Ready, *Effects of High-Power Laser Radiation*, Academic Press, Cambridge, Massachusetts (1971).
2. B. Zohuri, *Directed Energy Weapons: Physics of High Energy Lasers (HEL)*, Springer International Publishing, New York (2016).
3. P. Sprangle et al., "High-power lasers for directed-energy applications," *Appl. Opt.* **54**(31), F201–F209 (2015).
4. Y. Izawa et al., "High power lasers and their new applications," *J. Opt. Soc. Korea* **12**(3), 178–185 (2008).
5. H. Injeyan and G. D. Goodno, *High Power Laser Handbook*, McGraw-Hill, New York (2011).
6. J. W. Dawson et al., "Analysis of the scalability of diffraction-limited fiber lasers and amplifiers to high average power," *Opt. Express* **16**(17), 13240–13266 (2008).
7. C. Jauregui, J. Limpert, and A. Tünnermann, "High-power fibre lasers," *Nat. Photonics* **7**, 861–867 (2013).
8. M. N. Zervas and C. A. Codemard, "High power fiber lasers: a review," *IEEE J. Sel. Top. Quantum Electron.* **20**(5), 0904123 (2014).
9. Q. Fang et al., "5 kW near-diffraction-limited and 8 kW High-brightness monolithic continuous wave fiber lasers directly pumped by laser diodes," *IEEE Photonics J.* **9**(5), 1506107 (2017).
10. G. D. Goodno et al., "Coherent combination of high-power, zigzag slab lasers," *Opt. Lett.* **31**(9), 1247–1249 (2006).
11. L. Sun et al., "10.8 kW, 2.6 times diffraction limited laser based on a continuous wave Nd:YAG oscillator and an extra-cavity adaptive optics system," *Opt. Lett.* **43**(17), 4160–4163 (2018).
12. T. Y. Fan, "Laser beam combining for high-power, high-radiance sources," *IEEE J. Sel. Top. Quantum Electron.* **11**(3), 567–577 (2005).
13. N. Satyan et al., "Coherent power combination of semiconductor lasers using optical phase-lock loops," *IEEE J. Sel. Top. Quantum Electron.* **15**(2), 240–247 (2009).
14. H. Bruesselbach et al., "Self-organized coherence in fiber laser arrays," *Opt. Lett.* **30**(11), 1339–1341 (2005).
15. M. Wickham et al., "Coherently coupled high power fiber arrays," in *Adv. Solid-State Photonics*, p. MA4 (2004).
16. R. K. Huang et al., "High-brightness wavelength beam combined semiconductor laser diode arrays," *IEEE Photonics Technol. Lett.* **19**(4), 209–211 (2007).
17. T. H. Loftus et al., "Spectrally beam-combined fiber lasers for high-average-power applications," *IEEE J. Sel. Top. Quantum Electron.* **13**(3), 487–497 (2007).
18. B. Chann et al., "Near-diffraction-limited diode laser arrays by wavelength beam combining," *Opt. Lett.* **30**(16), 2104–2106 (2005).
19. A. Brignon, *Coherent Laser Beam Combining*, Wiley-VCH, Weinheim, Germany (2013).
20. J. W. Goodman, *Introduction to Fourier Optics*, McGraw-Hill, New York (1996).
21. F. M. Dickey, *Laser Beam Shaping: Theory and Techniques*, CRC Press, Boca Raton, Florida (2014).
22. T. S. Ross, *Laser Beam Quality Metrics*, SPIE Press, Bellingham, Washington (2013).
23. P. Zhou et al., "Numerical analysis of the effects of aberrations on coherently combined fiber laser beams," *Appl. Opt.* **47**, 3350–3359 (2008).
24. P. Gontar and J. K. Jabczynski, "Tolerance analysis of coherent combining optical system," *Proc. SPIE* **10976**, 1097615 (2018).

25. C. D. Nabors, "Effects of phase errors on coherent emitter arrays," *Appl. Opt.* **33**(12), 2284–2289 (1994).
26. J. B. Shellan, "Phased-array performance degradation due to mirror mis-figures, piston errors, jitter, and polarization errors," *J. Opt. Soc. Am. A* **2**(4), 555–567 (1985).
27. H. Zügge et al., *Handbook of Optical Systems, Volume 3: Aberration Theory and Correction of Optical Systems*, Wiley VCH, Weinheim, Germany (2007).
28. P. Zhou et al., "Tolerance on tilt error for coherent combining of fiber lasers," *Chin. Opt. Lett.* **7**(1), 39–42 (2009).

Przemyslaw Gontar is a PhD student at MUT. He received his MSc Eng degree in nanoengineering from Wroclaw University of

Technology in 2017. He has been with the Institute of Optoelectronics since 2017. His current research interests include high-power laser systems.

Jan K. Jabczynski is a full professor at Military University of Technology (MUT), Warsaw, Poland. He received his MSc Eng, PhD, and DSc degrees in 1981, 1989, and 1997, respectively. Since 1982, he has been a worker at the Institute of Optoelectronics, MUT. He has been a tutor of applied optics, laser optics, and propagation at MUT. His current research interests include laser optics, coherent optics, high-power laser systems, and diode-pumped lasers.